Skin stimulation and recording: Moving towards metal-free electrodes

11 (2022) 100143

Contents lists available at ScienceDirect

Biosensors and Bioelectronics: X

journal homepage: www.journals.elsevier.com/biosensors-and-bioelectronics-x

Skin stimulation and recording: Moving towards metal-free electrodes

Sebastian W. Shaner [a,b,*], Monsur Islam [c], Morten B. Kristoffersen [f,i], Raheleh Azmi [d], Stefan Heissler [e], Max Ortiz-Catalan [f,g,h,i], Jan G. Korvink [c], Maria Asplund [a,b,j,k,**]

[a] Department of Microsystems Engineering (IMTEK), University of Freiburg, Freiburg, Germany
[b] BrainLinks-BrainTools Center, University of Freiburg, Freiburg, Germany
[c] Institute of Microstructure Technology (IMT), Karlsruhe Institute of Technology, Eggenstein-Leopoldshafen, Germany
[d] Institute of Applied Materials, Energy Storage Systems (IAM-ESS), Karlsruhe Institute of Technology, Eggenstein-Leopoldshafen, Germany
[e] Institute of Functional Interfaces (IFG), Karlsruhe Institute of Technology, Eggenstein-Leopoldshafen, Germany
[f] Center for Bionics and Pain Research, Sweden
[g] Department of Electrical Engineering, Chalmers University of Technology, Sweden
[h] Operational Area 3, Sahlgrenska University Hospital, Mölndal, Sweden
[i] Department of Orthopaedics, Institute of Clinical Sciences, Sahlgrenska Academy, University of Gothenburg, Sahlgrenska University Hospital, Gothenburg, Sweden
[j] Division of Nursing and Medical Technology, Luleå University of Technology, Luleå, 97187, Sweden
[k] Freiburg Institute for Advanced Studies (FRIAS), University of Freiburg, Freiburg, Germany

ARTICLE INFO

Keywords:
Bioelectronics
Conducting hydrogels
Direct current stimulation
Skin electrodes

ABSTRACT

When one thinks about electrodes, especially ones meant for humans, one typically thinks of some kind of metal. Whether on the skin or in the brain, metal electrodes are characteristically expensive, stiff, non-efficient in electron-ion transduction, and prone to toxic metal ion by-products during stimulation. In order to circumvent these disadvantages, electrically-conductive laser-induced graphene (LIG) and mixed electron-ion conducting polymer (poly(3, 4-ethylenedioxythiophene) polystyrene sulfonate – PEDOT:PSS) was leveraged to create a metal-free electrode combination that allows for an economical, soft, and organic electrode for applications on human skin. Compared to clinical-standard silver – silver chloride (Ag/AgCl) skin electrodes, the metal-free hydrogel electrodes show notable improvement in electrochemical stability and prolonged stable potentials during long-term DC stimulation (0.5–24 h). Recording and stimulation performance on human participants rivals that of Ag/AgCl, thus fortifying the notion that they are an appropriate progression to their noble metal counterparts.

1. Introduction

Electricity plays an integral role throughout the human body, from nervous system transduction to wound-induced electrical fields. In bioelectronic medicine these electrophysiological signals are linked to external devices which are used to diagnose, treat or rehabilitate patients (Thakral et al., 2013; Takeda et al., 2017; Hong and Lieber, 2019). There are quite a few standard procedures that record biological electric potentials or stimulate tissue and nerves. The more common clinical stimulation procedures include transcutaneous electrical nerve stimulation (TENS) and transcranial direct current stimulation (tDCS). Notable biopotential recording methods include established procedures like electrocardiography (ECG), electromyography (EMG), and electroencephalography (EEG) as well as newer applications like neuroprosthetics. An ideal neuroprosthetic would allow for bidirectional communication (*i.e.,* recording and stimulation) between the body's nervous system and the prosthetic. For it is the electrodes that are the physical and electrical nodes between both systems and act as gateways between the organic (*i.e.,* tissue) and inorganic (*i.e.,* electronics) worlds.

Typically, skin electrodes are divided into two categories: wet versus

Abbreviations: LIG, laser-induced graphene; PP_f, electropolymerized PEDOT/PSS film; PP_h, pipette-casted PEDOT:PSS dispersion formed into hydrogel; Ag/AgCl, silver/silver chloride.

* Corresponding author. Department of Microsystems Engineering (IMTEK), University of Freiburg, Georges-Köhler-Allee 201, 79110, Freiburg im Breisgau, Germany.

** Corresponding author. Department of Microsystems Engineering (IMTEK), University of Freiburg, Georges-Köhler-Allee 201, 79110, Freiburg im Breisgau, Germany.

E-mail addresses: sebastian.shaner@brainlinks-braintools.uni-freiburg.de (S.W. Shaner), maria.asplund@imtek.uni-freiburg.de (M. Asplund).

https://doi.org/10.1016/j.biosx.2022.100143
Received 27 December 2021; Received in revised form 24 March 2022; Accepted 4 April 2022
Available online 13 April 2022

dry. This depends on if they are to be used with or without an additional electrolyte gel applied between the electrode and the skin. Wet electrodes (*e.g.,* silver-silver chloride – Ag/AgCl, with a sodium chloride-based electrolyte gel) are beneficial in that the electrochemical reactions between the electrode and the gel are well-defined and that the electrode system is non-polarizable, thus making it resilient to interference, such as noise and/or movement artifacts. Practically, they are limited in clinical settings as the electrode will decompose during stimulation and the electrolyte can dry out over longer usage times, in turn leading to signal deterioration. Furthermore, electrolyte gels can cause complications (*e.g.,* evaporation and skin irritation) during long-term measurements (Lee and Kruse, 2009; Thakor, 2015). Dry electrodes (*e.g.,* 304 stainless steel or Ag/AgCl) are used without any electrolyte, but are nevertheless saturated by the sweat of the patient. While they are more practically convenient and more comfortable for the patient, the disadvantage is that they may polarize, have higher impedance with the skin, and are less well-defined electrochemically. Consequently, dry electrodes are more sensitive to interference and patient variability. Age, gender, and ethnicity all affect the dryness and structure of the skin, which leads to a wide variety of impedance values.

Either wet or dry, the inherent problem of typical metal electrodes is the same. That is, they are poor ionic conductors and it is with ions that current flows within tissue. Electrochemical reactions determine if and how signals cross the metal-tissue interface, which generally results in high contact impedance and electrode corrosion. During stimulation, electrodes like Ag/AgCl rely on the outermost salt layer (AgCl) to dissociate into Cl-ions, so that electronic current from the bulk Ag can transition to ionic current within the gel and propagate to the skin. Metals and alloys that are corrosion-resistant, are generally too expensive to allow for fully disposable electrodes.

In recent years, progress has been made towards developing new classes of metal-free materials based on carbon and other conducting polymers. Previously, carbon-based electrodes used for biopotential recording have be fabricated using graphene, carbon black, glassy carbon, or carbon nanotubes (Das et al., 2017; Noh et al., 2016; Vomero et al., 2017; Kim et al., 2018). Among these, all were able to have comparable or improved biopotential recording when juxtaposed to the clinical-standard metal electrode of the respective application, including Ag/AgCl. Of particular focus, the recent discovery of laser-induced graphene (LIG) in 2014 provided straight-forward fabrication of a 3D porous graphene-like carbon that can be easily patterned on a variety of planar and curved organic materials (Ye et al., 2019). However, these prior carbon-based systems did not demonstrate the ability to also stimulate, which can be important for future human-interfacing systems that require electrical feedback. Alternatively, intrinsically conducting polymer (CP) films are attractive replacements to metal and carbon electrodes. The most common CP films are poly(3, 4-ethylenedioxythiophene) (PEDOT), polyaniline (PAni), and polypyrrole (PPy), or composites with these CPs as the conductive basis of the film (Bredas and Street, 1985; Balint et al., 2014). The hybrid charge transfer properties of CP based films, facilitate charge transfer between electrode and tissue which generally renders CP electrodes highly efficient, specifically the ionomer combination of PEDOT with polystyrene sulfonate (PSS) (Naveen et al., 2017; Gueye et al., 2020). In addition, CPs can be biofunctionalized and mechanically adapted to improve their properties as skin interfaces making them more versatile than carbon electrodes. There also exists conducting polymer hydrogels, which are similar in nature to CP films. However, they retain a high-level concentration of water, are hydrophilic in nature, and typically have mechanical properties (*e.g.,* Young's modulus) on par with human tissue (Tomczykowa and Plonska-Brzezinska, 2019; Wirthl et al., 2017; Yuk et al., 2019). The vast majority of CP hydrogels are largely comprised of an insulating network. Nevertheless, it is possible to generate conducting polymer hydrogels based purely on PEDOT:PSS thereby ensuring all parts are part of the electroactive system, which was conceptually demonstrated already in 1998 for ionically-crosslinked conducting hydrogel electrodes (Ghosh et al., 1998).

The application of merging carbon-based electrode (for its base electrode processability) and CP-based electrode (for its mixed ion-electron conductivity for tissue interfacing) is not new (Bareket et al., 2016). Others have used this kind of combination for recording potentials invasively and noninvasively, but have yet to successfully use it for dual communication with the body across the skin barrier (*i.e.,* skin-based stimulation in conjunction with recording). Whether the application requires short stimulation pulses (*e.g.,* prosthetic arms) or more stressful long stimulation pulses (*e.g.,* tDCS), there is room for innovation. The twofold capability for the same material combination to reliably record or stimulate, all the while allowing for non-cleanroom fabrication with cheap and sustainable materials, is the crux of this work.

In this study, combining LIG and PEDOT:PSS hydrogels was investigated. Specifically, LIG acting as the base electrode material and conductive hydrogels functioning as the skin-interfacing active sites. LIG stands out as a compelling approach for base electrode fabrication as it allows devices to be fabricated in a cheap and reproducible manner using a commercial carbon dioxide (CO_2) laser (Mamleyev et al., 2019). LIG is a respectable candidate for recording and stimulation, however the initial non-faradaic current generated during direct current (DC) stimulation requires relatively high potentials, which could require the need for electrolyte gels. This is where PEDOT:PSS can provide better mixed ion-electron conductivity. Recent work showed an important next step towards stable hydrogels purely comprised of PEDOT:PSS without the need for an insulating hydrogel scaffold (Lu et al., 2019). In this work, the adhesion of PEDOT:PSS hydrogels to LIG via some surface modifications (*i.e.,* amination and polyurethane dip-coating) were paramount to generating a stable physical and electrical link between the interfacing electrode materials. This linkage between the design flexibility of LIG and excellent electrochemical properties of PEDOT:PSS hydrogel were verified by scanning electron microscopy (SEM), X-ray photoelectron spectroscopy (XPS), and Raman spectroscopy and evaluated via electrochemical (*i.e.,* high-cycle cyclic voltammetry and long-term DC stimulation) and mechanical (*i.e.,* wet-state bend testing) stress tests. The electrodes were then ultimately tested on human participants to assess their ability in recording (*i.e.,* myoelectric pattern recognition) and stimulation (*i.e.,* threshold tests). All of which were compared to commercial Ag/AgCl electrodes.

Note that throughout this work the difference between PEDOT and PSS deposition methods are as follows: electropolymerized PEDOT/PSS film = PP_f and pipette-casted PEDOT:PSS dispersion formed into hydrogel = PP_h. Also note that the "/" vs. ":" between PEDOT and PSS highlight the entirely different formation of PEDOT and PSS networks: electrochemical deposition versus solution-based dispersion, respectively.

2. Experimental section/Methods

All the following chemicals were purchased from Sigma Aldrich, unless otherwise noted.

2.1. Laser carbonization of polyimide films

Laser irradiation was performed on a commercial polyimide film (DuPont Kapton HN, USA) with a thickness of 125 ± 13 μm using a 10.6 μm wavelength CO_2 laser engraver (ULS Versa Laser 3.50). This laser featured a spot size of ~120 μm. During laser carbonization, a raster mode was used with laser power of 12% (4.8 W), scanning speed of 12% (1.56 cm/s) in raster mode, pulse rate of 1000 pulses per inch (PPI), and 3 mm gap between laser and film.

Electrodes were made with both 3 mm and 10 mm diameter active site formats, the latter of which was used all the testing unless noted otherwise. Feature sizes down to 150 μm was obtainable, but not relevant for this study (Fig. 1a).

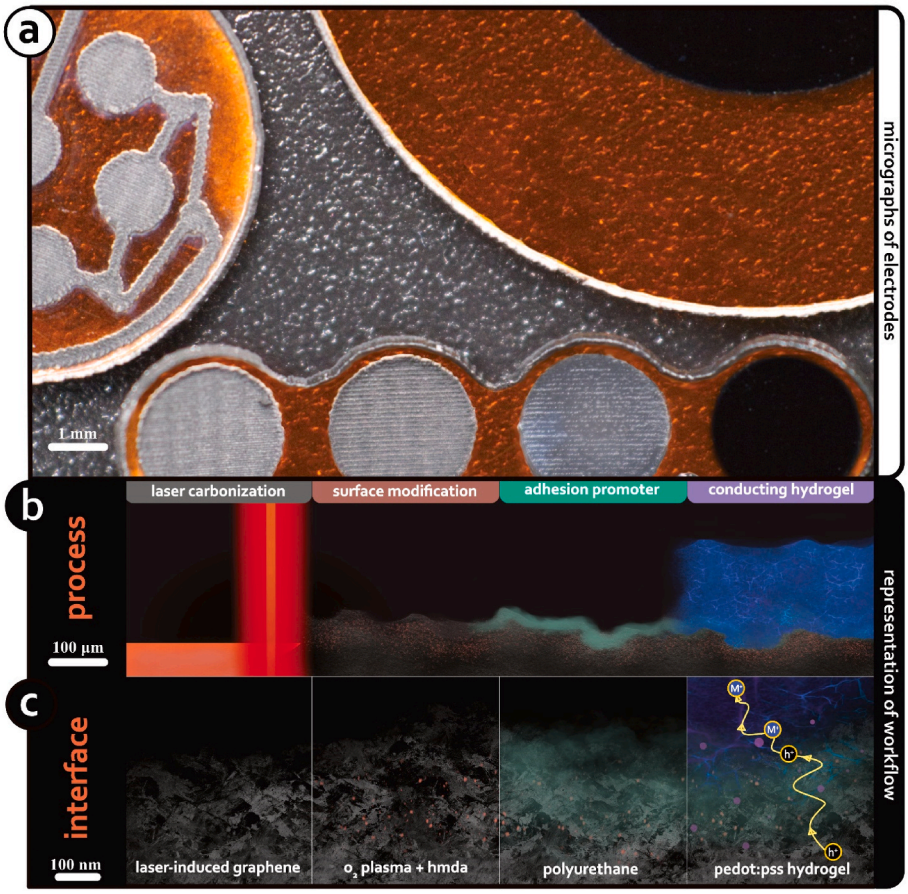

Fig. 1. Process to interface LIG to pure PEDOT:PSS hydrogel. (a) examples of feasible LIG electrode feature sizes with staged electrodes with different coatings – scale bar, 1 mm. **(b)** diagram showing process flow from left to right to go from a commercial polyimide sheet to supercapacitive hydrogel electrode in four steps – scale bar, 100 µm. **(c)** illustration of the interface between LIG and PEDOT:PSS hydrogel with an example current path during forward voltage that shows hole (h^+) transport through the LIG and into electronically-conductive PEDOT-rich domain and transitioning into the ionically-conductive PSS junctions to replace the cation (M^+) transport leaving the PEDOT:PSS hydrogel into the surrounding electrolyte – scale bar, 100 nm.

2.2. Surface-functionalization of LIG

Cleaning of the LIG electrodes entailed a wash step with acetone, IPA, and deionized (DI) water, then dried with nitrogen. O_2 plasma was subsequently performed at 100 W for 5 min at 10 sscm (Diener Electronic Femto Model 1, Germany). Amination of the plasma-treated electrodes was completed via immersion in 10% w/v hexamethylenediamine (HMDA) solution for 4 h at room temperature. Subsequent DI water rinsing was done to wash away unreacted HMDA, then dried with nitrogen. It was also possible to add $–NH_2$ groups onto the LIG via immersion in 1% v/v (3-aminopropyl)trimethoxysilane (*i.e.,* APTMS) solution for 60 min at room temperature. However, the electrodes used in this paper were done with the HMDA-treatment.

Polyurethane (AdvanSource HydroMed D3, USA) was deposited onto HMDA-treated LIG electrodes using a dip-coater (Nadetech ND-DC Dip Coater, Spain). PU was dissolved in ethanol (90%) to a final PU concentration of 1% w/v. The PU is covalently bonded to the amine groups on the treated LIG electrodes. The dip-coating (Nadetech NC-DC Dip Coater, Spain) immersion speed of 300 mm/min and retraction speed of 10 mm/min. Electrodes were then place on hot plate at 80 °C for 60 min to evaporate the solvent and solidify the PU adhesion (Inoue et al., 2020).

2.3. PEDOT:PSS electrodeposition and PEDOT:PSS hydrogel spot-casting, annealing and hydrogel formation

A commercial polyimide tape with silicone adhesive (DuPont Kapton 3M 5413, USA) was used as an insulation layer for the electrical trace layer. The adhesive side of the 69 µm thick film was O_2 plasma-treated at 30 W for 2 min at 10 sccm in order to add hydroxyl (-OH) groups to the silicone adhesive, which forms a strong bond to the electrode's amine-functionalized polyimide and LIG.

Electropolymerization was performed in a 3-electrode setup using a potentiostat/galvanostat instrument (Metrohm Autolab PGSTAT 204, The Netherlands). The working electrode (WE) was LIG, the counter electrode (CE) was a stainless-steel mesh with larger surface area than LIG active area, and the reference electrode (RE) was a standard Ag/AgCl electrode (BASI MF-2052, USA). The solution that the LIG electrodes were submerged into a glass container filled with 3,4-Ethylenedioxythiophene (EDOT, 10 mM) monomer and sodium polystyrene sulfonate (NaPSS, 5 mg/mL). Potentiostatic (+0.9 V) was applied until the charge reached 300 mC/cm^2, which takes about 10 min per electrode. The newly formed LIG/PP_f electrodes are then rinsed with DI water and stored in phosphate buffer saline (PBS, 10 mM) until experimental use.

Spot-casting of PEDOT:PSS dispersion starts with spiking dimethyl sulfoxide (DMSO) into the 1.3% stock PEDOT:PSS for a final DMSO concentration of 15% v/v. The thoroughly mixed PEDOT:PSS/DMSO solution is spot-casted onto the LIG/PU electrodes using a micropipette (5 µL for 3 mm diameter and 100 µL for 10 mm diameter electrodes). The aforementioned volume was the limit before the casted solution overflows onto the surrounding insulation interstitial area. The electrodes were then annealed on a hot plate for 12 h at 60 °C to evaporate the water and interpenetrate the PEDOT:PSS into the LIG/PU interface. A subsequent 130 °C step was done for 2 h to ensure DMSO evaporation and cause discontinuities in the PSS shells, which leads to more PEDOT-PEDOT junctions between adjacent segments (Lu et al., 2019). This allows for maintaining electrical connections throughout the swelling hydrogel during rehydration in PBS (0.01 M) to form the final LIG/PP_h electrode.

Two different deposition "thicknesses" were investigated for both the electrodeposited (thickness "a" and "2a") and spot-casted PEDOT:PSS

(thickness "b" and "2b"). The LIG/PP_f electrode thickness "a" had a lower cut-off charge (300 mC/cm^2) while "b" had a higher cut-off (600 mC/cm^2) and took twice as long. The two PP_f thicknesses were estimated to be 54 and 110 nm, by means of SEM analysis. The LIG/PP_h electrode thickness "b" was 50 μL of PEDOT:PSS/DMSO deposition solution and "2b" was 100 μL with no added processing time. The two PP_h (before rehydration) thicknesses were estimated to be 3.2 and 6.3 μm, by means of SEM analysis.

The deposition, annealing, and rehydration hydrogel process was much quicker at scale than the electropolymerization process since the former is a parallel method, while the latter is of a serial nature. For example, while the hydrogel process overall takes about 1.5-2X longer, the hands-on time is about 8X shorter than the electropolymerization method. Since the electrodes of interest are in the millimeter range, it was still feasible to do deposition via pipette-casting.

2.4. Surface chemical characterization

Raman spectroscopy of the LIG samples was performed on a Bruker Senterra set-up (equipped with a confocal microscope), using a DPSS laser ($\lambda = 532$ nm) at 2 mW power with a penetration depth of <1 μm.

XPS was performed using a micro-focused, monochromatic Al Kα X-ray source (400 μm spot size) on a K-alpha + XP spectrometer (Thermo Fisher Scientific). The data acquisition and processing for XPS were performed using Thermo Avantage software (Parry et al., 2006). The XPS spectra were fitted with one or more Voigt profiles. The binding energy uncertainty was around ±0.2 eV. The analyzer transmission function, Scofield sensitivity factors(Scofield, 1976), and effective attenuation lengths (EALs) for photoelectrons were applied for quantification. EALs were calculated using the standard TPP-2M formalism (Tanuma, 1994). The K-alpha + charge neutralizer was applied during measurements and since the sp^2 carbon species for all samples was observed at around 284.4 eV, no binding energy calibration was applied on the spectra.

2.5. Electrochemical and mechanical characterization

Cyclic voltammetry was performed using the same aforementioned 3-electrode setup and potentiostat. The potential was swept within the relevant water window, between −0.6 V and +0.9 V, for 5 cycles at 100 mV/s scan rate. The integral of the resulting CV profile gives the charge storage capacity (CSC), which quantifies how much charge the electrode can store in a specific voltage window.

2.6. Long-term DC stimulation

DC stimulation was carefully monitor using microfluidic device with a simple fluidic channel (i.e., resistor) connected between to media reservoirs. The microfluidic device was constructed of 5 total layers: (a) 1 mm thick glass microscope slide (b) 0.80 mm thick PMMA-based double sided pressure sensitive adhesive (dsPSA) with microchannel (c) 6 mm thick PMMA piece to add depth for the reservoirs (d) another dsPSA without microchannel and (e) 1 mm thick glass microscope slide. All PMMA layers were patterned using a CO_2 laser (Universal Laser Systems - ULS Versa 2.30 with $\lambda = 10.6$ μm). The microchannel was measured to be 450 μm wide, 80 μm tall, and 5 mm long. This cross-section of 0.036 mm^2 allows for easy calculation of the electric field seen within the channel (EF is the product of electrolyte resistivity and constant current divided by the microchannel's cross-section). The channel resistivity (function of channel volume and electrolyte resistivity) allows for simple calculation of voltage drop across the channel using Ohm's law for a given input current.

Once the microfluidic device was assembled, the electrodes were placed in the reservoirs and filled with PBS (0.01 M) and carefully making sure that the microchannel was void of air. A potentiostat/galvanostat was used to supply the constant current, which was 7.85 μA (i.e., 10 μA/cm^2 for the 10 mm diameter electrodes). Fresh PBS was exchanged between experiments.

2.7. Wet-state bend testing

Wet-state bend testing was implemented using a custom system. Three 3D printed parts (bend adapter, electrode holder, and viewing container) were used in conjunction with a commercial 3D printer (Prusa i3 MK3s, Czech Republic) to form the wet-state bend tester. The bend adapter is connected to the x-axis gantry of the printer, which attaches to the bottom of the electrode and provides the desired defection. The electrode holder is a two-part mating housing that sandwiches the electrodes and fixates it just above the electroactive site. The viewing container is a PET-G frame unto which 4 glass panels are placed and sealed with silicone at the joints. A simple G-code script was written using Notepad++, which was timed to concurrently run with a properly timed potentiostat CV protocol so that one script had a wait time while the other performed either the bending or CV.

2.8. EMG recording and stimulation on human participants

Participants (n = 6, mean age = 28.5, 3 females) were seated in front of a screen with their right forearm placed in a padded splint. Electrodes were placed equidistantly around the proximal part of the forearm. The two electrode types were placed next to each other in a crossed fashion, to achieve as similar recording area as possible. The Ag/AgCl reference electrode was placed on the lateral epicondyle (*i.e.,* the bony bump on the outside of the elbow). EMG was recorded at 2000 Hz using an open-source EMG acquisition hardware (Mastinu et al., 2017). The software used for recordings, processing, decoding/classification, and real-time testing was also an open-source platform called BioPatRec (Ortiz-Catalan et al., 2013).

Participants were asked to execute six movements (open hand, close hand, flex hand, extend hand, pronation, and supination) three times each for 3 s and with a 3 s resting phase between each repetition. EMG from both electrode types were recorded simultaneously, so that the generated EMG between the electrode types were equivalent. Signal processing was performed as commonly done in myoelectric pattern recognition (Ortiz-Catalan et al., 2013). Briefly, the transient part of the EMG was removed by omitting the first and last 15% of each repetition. The EMG signals was then segmented into 200 ms overlapping time windows with a 50 ms time increment. Four features were calculated per time window (mean absolute value, slope sign changes, zero crossings and wavelength) and used to train a linear discriminant analysis classifier. After the classifier was trained, the participant performed a Motion Test as implemented in BioPatRec (Ortiz-Catalan et al., 2013; Kuiken et al., 2009). In the Motion Test, participants were prompted to match a requested movement. Each prompted movement counted as a trial and for a successful trial the output of the classifier had to match the prompted movement for 1 s within a 10 s timeout. The Motion Test consisted of 30 trials and was performed once per electrode type. The electrode order was randomized between participants and participants were blinded to which electrode was being tested.

For the electrotactile stimulation, two of the same electrodes used for EMG recording placed on the volar side of the forearm were used. The electrodes were connected to a DS5 Isolated Bipolar Constant Current Stimulator (Digitimer Ltd, United Kingdom). The DS5 was connected to a custom-made neurostimulator, which was controlled using experiment-specific MATLAB script (Mastinu et al., 2017). Stimulation frequency was 100 Hz and the pulse width of 250 μs with a cathode-first asymmetric charge-balanced square wave. The starting amplitude was determined by giving a 1 s pulse at 750 μA and manually reducing the amplitude by 100 μA until the participant no longer felt the stimulation after which it was increased by 50 μA. When the starting amplitude was determined, the perception threshold was measured using the two-interval forced-choice method where they received two prompts. In

one of the prompts they received stimulation and in the other they did not (null stimulus). The participant was asked to identify the prompt with stimulation. When the participant chose a prompt, they received two new prompts where the stimulation was decreased if they selected the correct prompt or increased if they chose the wrong prompt. Participants were not notified if they gave the correct response or not. Each participant received 20 prompts per electrode type. The stimulation was modulated according to a stochastic approximation staircase approach (Faes et al., 2007). The test was performed once per electrode type and participants were blinded to the electrode type being tested.

All human participants provided written consent and testing was approved by the Swedish Ethical Review Authority (No. 2020–06500).

3. Results

3.1. Impact of surface treatments on laser-induced graphene

The first step in the generation of metal-free skin electrodes is the carbonization of a polymer substrate into a conducting surface. Carbonization of polyimide (PI) films was accomplished by using a CO_2 laser ($\lambda = 10.6$ μm) to directly pattern and transition the insulative PI into conductive LIG. After laser carbonization, O_2 plasma surface treatment was performed to increase hydrophilicity of the natively hydrophobic LIG, which was essential to have rapid access to electrolyte and yield new functional groups for future processing (Fig. 1). Ensuing amine-functionalization (via hexamethylenediamine – HMDA) and polyurethane (PU) coating prepped the LIG surface with an adhesion-promoting, yet conductively-inducive interconnection between LIG and the eventual PEDOT:PSS coating (Inoue et al., 2020).

SEM micrographs of the LIG films reveals the porous nature of the newly created material, which is typical for LIG materials (Fig. 2a). (Mamleyev et al., 2020) After a 5 min O_2 plasma treatment there were no considerable changes observed in the morphology of the LIG sample (Fig. S1). This change to a hydrophilic surface was vital for all downstream processes in this work, from the functionalization of LIG to the deposition of PEDOT:PSS. The hydrophilicity was investigated using a contact angle goniometer. The untreated LIG sample features a hydrophobic surface with a contact angle of $95.3° \pm 1.9°$. The change to a hydrophilic surface after plasma treatment results from the uptake of oxygen molecules, which facilitates formation of hydrogen bonds with water molecules, resulting in lower contact angle. Furthermore, longer plasma treatment yielded lower contact angle. The contact angle decreased from $49.8° \pm 1.0°$ for 30 s of plasma treatment to $21.0° \pm 2.8°$ for 300 s (Fig. S1).

Raman spectra of plasma-treated LIG samples with varying plasma duration validated that the O2 plasma treatment had no additional effects on the LIG itself, aside from serving as a surface energy treatment (Fig. 2d, Fig. S1). The carbon characteristic peaks were seen at around

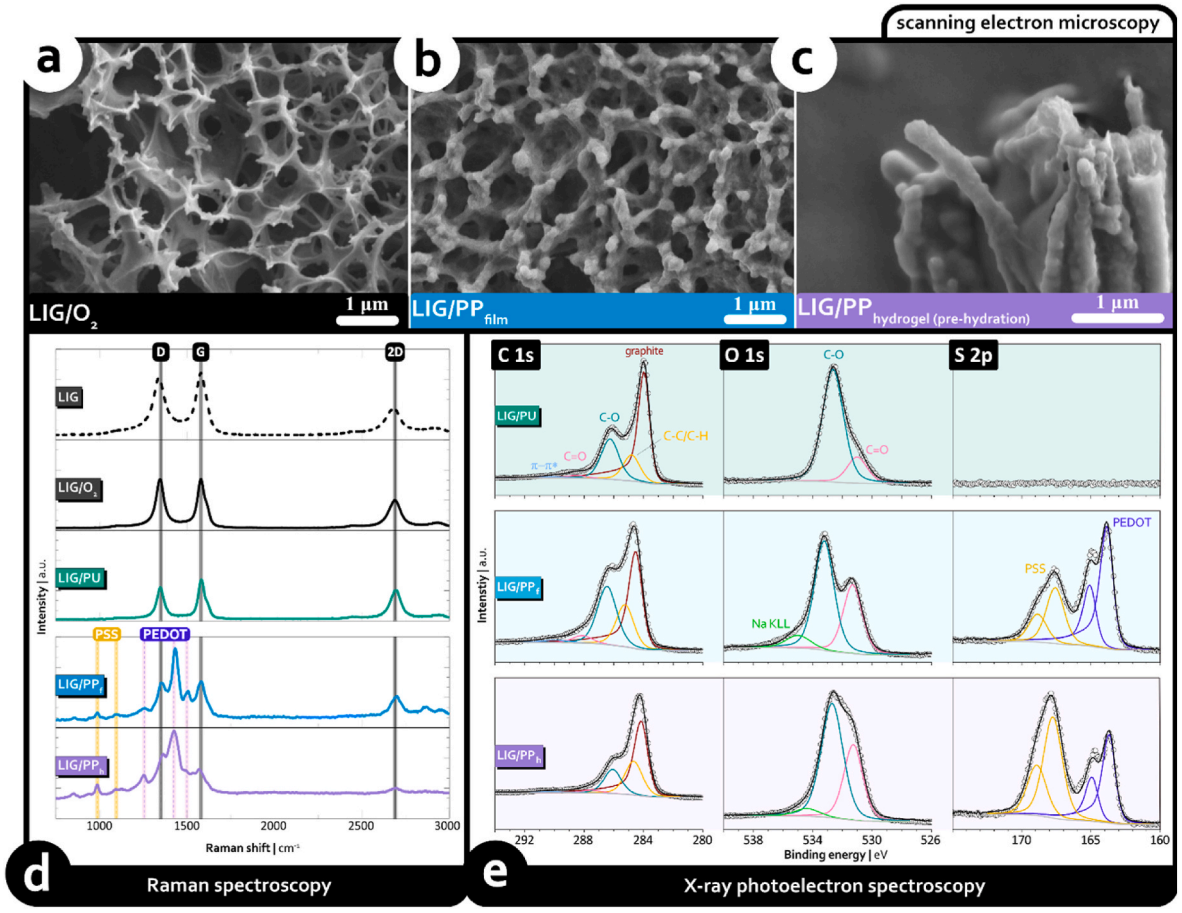

Fig. 2. Surface characterization of LIG and LIG/PEDOT:PSS (electrodeposition vs. solvent-casted) electrodes. (a) SEM image of LIG after O_2 plasma treatment. **(b)** SEM image of LIG/PP_f shows how PEDOT/PSS grows nodules on the pointed edges of the superficial LIG. **(c)** SEM image of annealed LIG/PP_h shows how casted PEDOT:PSS dispersion anneals over the LIG. In the background a smooth PEDOT:PSS surface is realized and how the annealed film typically coats the LIG surface. All scale bars for SEM images are 1 μm. **(d)** Raman spectra of electrodes at different stages of the process showing the graphene-rich carbon due to I_D/I_G and I_{2D}/I_G ratios of 0.9 and 0.5. Also, both LIG/PP_f and LIG/PP_h show the characteristic PEDOT and PSS peaks, where the thinner PP_f shows more underlying influence from LIG. **(e)** XPS analysis highlighting the C1s, O1s, and S2p spectra. The C1s spectrum shows high occurrence of C═C for all cases, which verifies LIG presence at the surface. The O1s spectrum shows that LIG samples show that the PEDOT:PSS coating causes a C═O peak increase. The S2p spectrum shows PP_f has more PEDOT than PSS, where it is the opposite for PP_h.

1350 cm^{-1}, 1580 cm^{-1}, and 2690 cm^{-1}, which are typically indexed to D (A_{1g} breathing mode, resulted from disorder in sp^2 carbon), G (E_{2g} mode, responsible for the stretching vibrations in all sp^2 carbons) and 2D peak (characteristic of sp^2 carbon), respectively (Mamleyev et al., 2020; Wang et al., 1990). For the untreated LIG sample, an I_D/I_G ratio around 0.9 and an I_{2D}/I_G ratio around 0.5 were obtained, which suggests formation of highly graphene-rich carbon during laser irradiation. Similar I_D/I_G and I_{2D}/I_G were also obtained for all the plasma-treated samples and adhesion promotion steps. This further cement the notion that the LIG surface maintains it graphene-rich nature, while also gaining hydrophilicity after plasma exposure.

The surface was further characterized by using X-ray photoelectron spectroscopy (XPS) demonstrating the formation of new functional groups on the LIG surface after all adhesion promotion steps and PEDOT:PSS deposition. The C1s spectra of all LIG samples (before any PEDOT:PSS was added) featured asymmetric line-shape of sp^2 carbon (~284.5 eV) and π-π* shakeup satellite (~291.3 eV), which also confirms successful graphitization of the material (Fig. 2e, Fig. S1). The major peaks in the O1s spectra of the untreated LIG sample were assigned to aliphatic C═O (532.2 eV) and C–O (533.4 eV), whereas the low intensity peaks at higher binding energies are likely due to OH and water adsorbates on the surface (535–536 eV) (Zielke et al., 1996). For untreated LIG and according to the O1s spectra, a weak contribution of residual C–O/C–N (285.8 eV) and C═O (288.2 eV) functional groups could be fitted in the C1s spectrum, although the deconvolution of weak C–O/C–N and C═O peaks in C1s spectrum considering the tailing of graphite peak is difficult. The concentration of oxygen-containing groups increased significantly after 30 s of O_2 plasma treatment of the LIG samples as shown in C1s and O1s spectra (Fig. S1). The C1s peak at 287.2 eV gained intensity, which corresponds to the C═O functional group, and this is matching with the gain of intensity on O1s spectra at around 532.4 eV (C═O) and 533.2 eV, (C O). The atomic concentration of the mentioned oxygen species increased from 6.5 at. % for untreated LIG to 12.7 at. % for 30 s O_2 plasma treatment. Further slight increase in the oxygen-containing functional groups was noticed when the plasma duration increased from 30 to 150 s (15.1 at. %). However, more plasma duration resulted in no noticeable increase of the oxygen containing functional groups on the LIG surface (Fig. S1).

3.2. Electropolymerization of PEDOT/PSS vs. spot-casting of PEDOT:PSS dispersion on LIG electrodes

In order to facilitate signal transmission at the skin-electrode interface, it is desirable to functionalize the LIG with a material that has mechanical and electrochemical properties close to that of skin. The use of electrodeposited PEDOT/PSS (PP_f) as a coating on metallic bioelectrodes is well established and known to enhance both the recording and stimulation properties of neural microelectrodes (Han et al., 2007; Asplund et al., 2010; Nasybulin et al., 2012). Additionally, the combination of LIG and PEDOT has previously shown promise as a dopamine sensing electrode (Xu et al., 2018). The expected weakest link is the adhesion stability of the PP_f to the rough LIG substrate, wherefore adhesion promotion is necessary to fully leverage the beneficial properties of PEDOT as an electrode interface (Inoue et al., 2020). Both the necessary adhesion promotion and exploration of two alternative deposition techniques were addressed in this work. Namely, electrodeposition of PEDOT/PSS (*i.e.,* bottom-up fabrication using EDOT monomer and sodium polystyrene sulfonate - NaPSS) and spot-casting (*i.e.,* using a pipette to precisely dispense known volume) of commercial PEDOT:PSS dispersion onto electrodes with subsequent annealing yields CP films with high conductivity. In brief, the pure PEDOT:PSS hydrogel (PP_h) is formed as follows: addition of dimethyl sulfoxide (DMSO) to the PEDOT:PSS dispersion solution promotes the dissolution of the PSS shells and during annealing the DMSO evaporates, which allows for a new arrangement of PEDOT and PSS with more PEDOT-PEDOT junctions (Lee et al., 2016). Upon rehydration, this material showed the characteristics of a conducting hydrogel (Lu et al., 2019). Thus, spot-casting is an attractive alternative to electrodeposition, as the process is easier to scale both in terms of parallelizable fabrication of electrodes and to enable thicker hydrogel coatings with increased charge storage capacity.

Both electrodeposition of PP_f and spot-casting, annealing, and rehydration of PP_h was performed on the PU-treated LIG electrodes (Fig. 2b and c). After the application of the PU adhesion promoter, the PP_f is electrodeposited onto the submerged conductive LIG in the presence of a solution of EDOT monomer and NaPSS in a potentiostatic (+0.9 V) 3-electrode setup. The longer the deposition, the thicker and more conductive the PP_f (Fig. 3b). From the SEM micrographs it can be seen that the sharp nodules of the LIG also translates to a similar, but more bulb-like nodule formation in the PEDOT/PSS (Fig. 2b). This is due to the higher current density at these sharper edges, thus resulting in a higher film growth rate on these locations. In contrast, the spot-casted and annealed PEDOT:PSS completely covers the underlying rough morphology of the LIG. Consequently, the intersection between the film and underlying LIG is not visible (Fig. 2c).

Even though SEM paints part of the picture, the XPS data of LIG/PU, LIG/PP_f (thick), and LIG/PP_h (thin) electrodes reveal the surface chemistry after the addition of adhesion promotion layers (hexamethylenediamine - HMDA and polyurethane - PU) and PEDOT:PSS layers (Fig. 2e). Due to the of the porous nature of the LIG, the graphite peak is still detectable by XPS after adding HDMA, PU, PP_f, and PP_h layers in C1 spectra. The C–O and C═O species related to the PU, PEDOT, and PSS can be found at around 286.5 and 288 eV of C1s spectra. Related oxygen peaks can be found at around 531.3 and 532.8 eV for C═O and C–O, respectively. The oxygen peak related to $–SO_3$ species of PSS polymer is as well overlapped to C═O peak at around 531.3 eV. Due to the use of NaPSS, some Na contamination is also detected on PP_h samples at around 1071.5 eV, such that the Na KLL Auger peak can also be detected in the O1s spectra of these samples. The C–NH bonding of PU is detectable in N1s spectrum at around 399.5 eV showing its successful deposition (Fig. S2).

In the S2p spectrum, the C–S–C bonds of PEDOT at around 163.9 eV ($S2p_{3/2}$) and 165.1 eV ($S2p_{1/2}$) can be detected, as well as the $–SO_3$ species of PSS at around 167.6 eV ($S2p_{3/2}$) and 168.9 eV ($S2p_{1/2}$) (Zhang et al., 2013; Kleber et al., 2017; Greczynski et al., 1999). The S2p doublet of PEDOT is deconvoluted with an asymmetric tail on the higher binding energy side according to the ansatz of Bae et al. arguing that the charge distribution on partly oxidized PEDOT-chain results in a broad distribution of binding energies for the sulfur atoms (Bae et al., 2016). In contrast, the LIG/PU sample has a negligible signal, which shows the sulfur peaks are solely related to the added PEDOT and PSS. The electronegativity difference of S–C (PEDOT) and S–O (PSS) bonds allows unambiguous differentiation of these two polymers and since there is only one sulfur atom per monomer of each polymer, one can directly compare the amount of deposited PEDOT to PSS in each deposition method (Bae et al., 2016). As expected, the PSS content is higher than the PEDOT content (PEDOT to PSS = 0.7) for the spot-casted and annealed PEDOT:PSS dispersion (LIG/PP_h). Whereas, in the electrodeposited PEDOT:PSS film (LIG/PP_f), the PEDOT content was higher than the PSS (PEDOT to PSS = 1.9).

Furthermore, the Raman characteristic peaks of both PEDOT and PSS help confirm that PP_f has accessible LIG, which is noticed by the 2D peak indicating that the carbon is accessible under the thin superficial layer (Fig. 2d).

3.3. Improvement of charge storage capacity of LIG by means of PEDOT:PSS hydrogel coating

Through cyclic voltammetry (CV) it is possible to estimate the charge storage capacity (CSC) of the electrode, which is expected to correlate with the amount of electroactive polymer available on the surface (Leal et al., 2021). In addition, by subjecting the electrode complex to a large

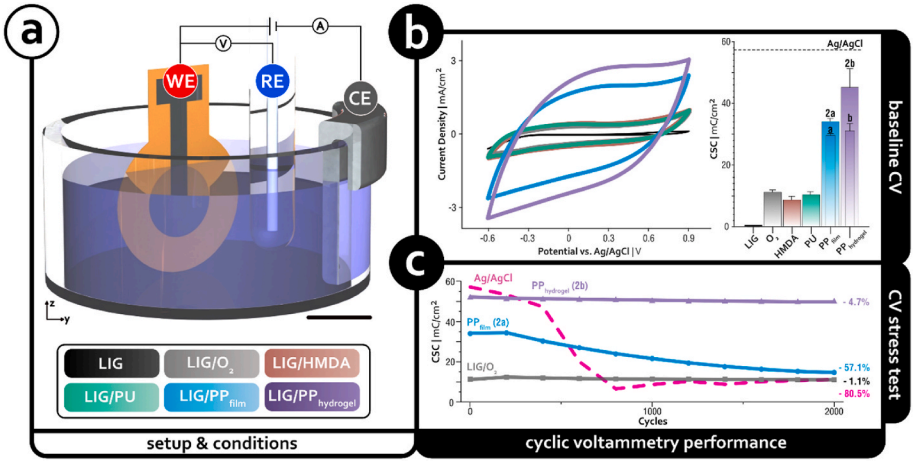

Fig. 3. Cyclic voltammetry baseline and stress test. (a) Three-electrode setup in a phosphate-buffered saline (PBS, 10 mM) filled glass container with the test electrode of interest being the working electrode. The test electrode conditions were native LIG, oxygen-plasma treated LIG (LIG + O_2), amine-functionalized LIG (LIG + O_2+HMDA), polyurethane-coated LIG (LIG + O_2+HMDA + PU), electrodeposited PEDOT/PSS on LIG (LIG + O_2+HMDA + PU + PP_f), and spot-casted PEDOT:PSS hydrogel on LIG (LIG + O_2+HMDA + PU + PP_h) **(b)** Cyclic voltammetry (CV) profiles and corresponding charge storage capacity (CSC) values for all test electrodes showing that both PP_f and PP_h significantly improve the CSC. **(c)** CV stress test of 2000 cycles comparing new LIG and PEDOT:PSS combinations to commercial Ag/AgCl EMG electrodes establishing that LIG and LIG/PP_h possess superior electrochemical stability to Ag/AgCl. Scale bar is 10 mm. WE = working electrode. RE = reference electrode. CE = counter electrode.

number of charge-discharge cycles (*i.e.,* number of CV scans) the measurement provides insight in to the ability of the material to withstand repeated electrochemical load without deterioration of its qualities (Boehler et al., 2020). For PP_h, the amount of material can be controlled directly in the spot-casting, while for PP_f this is controlled indirectly by limiting the deposition charge. The CSC of the bare LIG is enlarged by the porous structure (Fig. 2a), and the addition of PP_f or PP_h increases the CSC even further. The resulting CSC improved (106%) from O_2 plasma-treated LIG (13 ± 2 mC/cm^2) to LIG/PP_f (27 ± 3 mC/cm^2). Whereas the PP_h increased the CSC (231%, 43 ± 6 mC/cm^2) as compared to LIG/O_2 (Fig. 3b). The oxidation and reduction of the LIG/PP_h during 5 cycles of CV gives initial insight into how well the electrode can handle the influx and outflux of ions within the conductive hydrogel matrix without delamination (Movie S1). Note that the geometrical surface area (GSA = 0.785 cm^2), based off the electrode's diameter, was used for CSC calculations. The electrochemical surface area (ECSA = 0.773 cm^2), based off of the Randles-Sevcik equation, was found to be comparable to the GSA (Fig. S3).

In order to further investigate the robustness of repeated and rapid electrochemical charging and discharging of ions, the electrodes were electrochemically stressed over 2000 CV cycles (−0.6 V to +0.9 V at 100 mV/s in 10 mM phosphate-buffered saline - PBS) monitoring the change in CSC over time. Without a coating, LIG electrodes have a comparably low CSC, but maintain an exceptionally stable performance and lose only 1.1% of their CSC throughout the full 2000 cycles. The LIG/PP_f electrodes start at a significantly higher CSC, but lose more than half of their CSC over the 2000 cycles, thus bringing them close to the CSC of the plasma-treated LIG. In contrast, the LIG/PP_h electrodes have both higher initial CSC and manage to maintain most of this throughout the cycling (95%). To put this number in perspective, Ouyang et al. reports on delamination within the first 100 cycles (Ouyang et al., 2017), whereas here the sustained high performance over 2000 cycles and beyond strongly support that the combination of materials presented successfully merges the high CSC of the conducting polymer hydrogel with the electrochemical stability of a carbon electrode. The difference between the two types of PEDOT:PSS materials can be understood by considering that the bulk PEDOT:PSS layer will swell and shrink throughout each CV cycle as ions will be exchanged with the surrounding electrolyte to compensate for the switching polarity (Persson et al., 2014). The electrodeposited PEDOT/PSS film (PP_f) is adhered to the loosely-bound superficial LIG layer, which has an easier likelihood to become delaminated during the quick swelling and shrinking during ion exchange. Whereas with the PEDOT:PSS hydrogel (PP_h), the stress (*i.e.,* at the electrode-electrolyte interface) is occurring much further from the LIG-PEDOT:PSS junction compared to the much thinner PP_f. It should here be noted that the stability of the hydrogel electrodes greatly exceeded that of commercial Ag/AgCl electrode: 96.3% vs. 19.5% CSC retention (Fig. 3a), over the 2000 cycles. This is not surprising since the Ag/AgCl will dissociate the Cl^- ions from superficial AgCl with every cycle as the reaction has poor reversibility under the conditions of a voltage sweep. Nevertheless, this comparison was selected because Ag/AgCl is one of the most common materials used for electrodes contacting the skin and thereby serves as reference material.

It is important to note that the deposition volume of PEDOT:PSS/DMSO was maxed out for each electrode size, such that the droplet rested on top of the electrode without overflowing onto the interstitial insulation (Fig. S4). With the above electrodeposition time constraints and the fixed hydrogel deposition volume under consideration, the PP_h coating with "2b" thickness was down-selected for all future investigations in this paper.

3.4. Wet-state mechanical bend testing of electrodes

While CV scans serve to demonstrate the electrochemical stability of the electrode complex, the use of electrodes on patient skin and during activities of daily living is expected to subject the electrodes to substantial mechanical load. As electrochemical stress tests cannot provide full insight into the longevity of the electrode material, application-dedicated mechanical tests were performed in order to demonstrate that these electrodes can maintain electrochemical performance during repeated movement (*e.g.,* patient's arm translation or rotation). Specifically, a submersion-based bend tester that utilizes a commercial 3D printer to act as the programmable axis control was built (Fig. 4). The wet-state environment allows for an in-situ combination of mechanical and electrochemical validation of the LIG/PP_h electrode interface. At the bottom of the 3D-printed electrolyte container there is a rigid structure unto which the neck of the electrode is mounted with the electroactive site free to move in the PBS (Fig. 4a and b). The electrical lead connection to the electrode's bump pad was just outside of the PBS so that connection to the potentiostat remained dry. A 3D-printed electrode holder was mounted to the 3D printer's moving head and attached to the submerged end of the electrode (Movie S2). The bending test program consisted of a back and forth ±45° bend cycle (0.5 s duration at 83 mm/s linear actuation/retraction) for a total of 1000 cycles, where after every 100 bend cycles the protocol was programmed to pause to perform a CV to gauge when failure (*i.e.,* sharp decrease in CSC) might occur.

The LIG/PP_h electrode maintained a robust physical and conductive adhesion even during the compression and tension flexion from bending and the periodic electrochemical load supplied during CV. In fact, even after a 1000 bending cycles there was greater than 95% retention of CSC

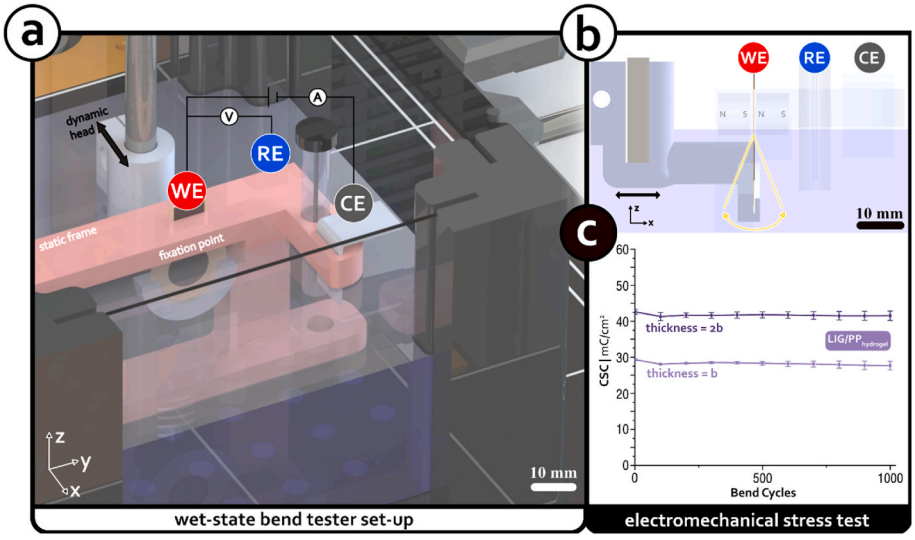

Fig. 4. Electromechanical stress test via wet-state bend testing and periodic cyclic voltammetry. (a) Three-electrode setup in large reservoir with working electrode attached to a translating arm, which is controlled with a three-axis CNC. **(b)** Cross-section of the setup showing how the electrode is bent. The electrode is sandwiched between two 3D-printed parts with embedded magnets along the electrode's connection trace, which connects the submerged electroactive area and the dry bump pad that is connected to the potentiostat. The dynamic head moves only along the x-axis, while the static frame keeps the electrode's bump pad and trace fixed in y & z. **(c)** This shows the electromechanical stress performance of LIG/PP_h electrodes of two different spot-casted volumes and their CSC as function of bend cycles, where one bend cycle is a ±45° deflection. Scale bars are 10 mm. WE = working electrode. RE = reference electrode. CE = counter electrode.

(Fig. 4c). Furthermore, robust adhesion was validated for both hydrogel thicknesses. In summary, both the electrochemical and mechanical analysis demonstrates that the material stack can withstand substantial loads, validates the efficiency of the adhesion promoting treatment, and thus confirms that the electrodes are well suited as a skin-electrode interface.

3.5. Long-term uni-directional vs. bi-directional direct current

Whereas typical neurostimulation electrodes mainly exploit pulses in the range of a few hundred microseconds, the signals used for stimulation over the skin covers the entire range from short pulses to direct current (DC). In particular, the latter is challenging for the electrodes because capacitive coupling cannot be used to deliver DC. The standard solution for DC is to use Ag/AgCl, which dissolves into its ions (Ag^+ and Cl^-) in order to supply the current. Here, PEDOT-based materials offer a considerable advantage as the large ionic pseudo-capacitance allows for delivery of DC in a faradaic, yet fully reversible, process. In order to explore the DC stimulation qualities of the LIG and PEDOT:PSS hybrid, a microfluidic device with two electrode/media reservoirs connected by a known fluidic resistor (*i.e.,* defined geometry) was fabricated. One reservoir would contain the anode and the other would hold the cathode, such that current is forced to travel through the rectangular microchannel (Fig. 5a, Fig. S5). This allows for precise knowledge of the contribution to the potential drop due to the electrode combination (*i.e.,* anode and cathode), as well as know the electric field in the microchannel.

Ag/AgCl, LIG, and LIG/PP_h electrodes (all with diameter of 10 mm) were used in the phosphate-buffered saline (PBS, 0.01 M) filled microfluidic setup. LIG/PPh electrodes were able to steadily (*i.e.,* no increasing potential) deliver current (10 and 25 μA/cm^2) for 24 and 20 h, respectively, with the same electrolyte used for the duration of the

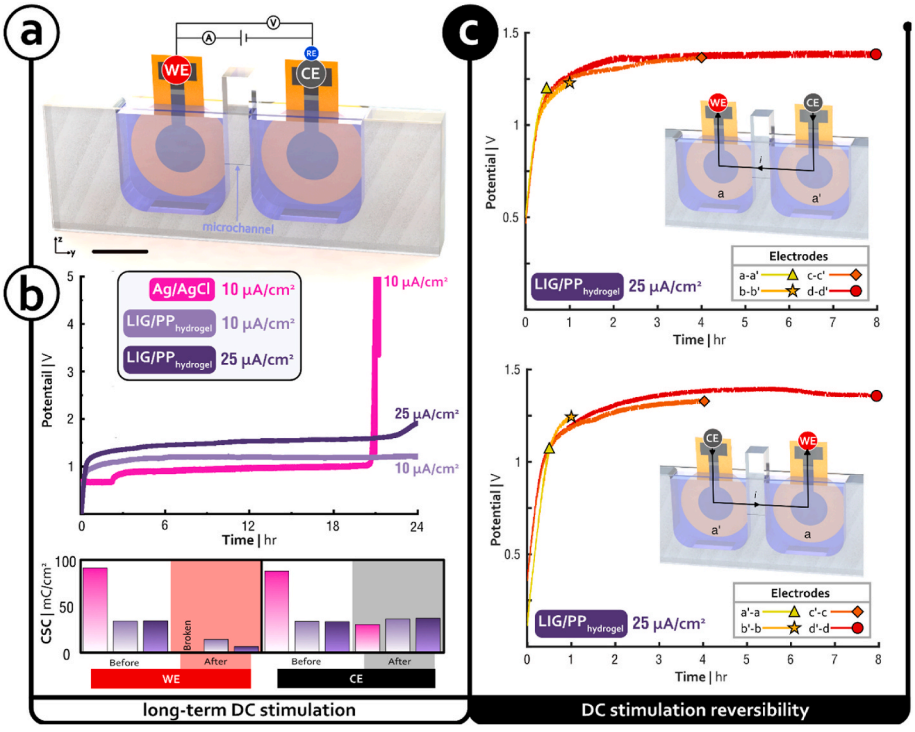

Fig. 5. Long-term uni- and bi-directional DC stimulation. (a) Two-electrode setup in two reservoirs connected by a microchannel of known dimensions (450 μm × 80 μm x 5 mm = width, height, and length, respectively). **(b)** Potential during 24 h of constant current DC stimulation. and the corresponding CSCs of the working (anode) and counter (cathode) electrodes before and after 24 h of stimulation. **(c)** The ability of LIG/PP_h electrodes to stimulate in one direction for 0.5, 1, 4, and 8 h, and immediately (in situ and same media) have the polarity switched and perform to the same length of galvanostatic DC stimulation (*e.g.,* electrode pair a-a' was stimulated for 0.5 h then the polarity was switched and stimulated for another 0.5 h. Scale bar is 10 mm. WE = working electrode. RE = reference electrode. CE = counter electrode.

experiment (Fig. 5b). The Ag/AgCl electrode had the lowest initial potential, however the potential was not as stable at 10 μA/cm^2 as compared to LIG/PP$_h$ and after 20 h of stimulation the electrodes completely disintegrated from the electrical leads rendering them useless for further measurements. In contrast to this, the CSC before and after DC stimulation confirms that the LIG/PP$_h$ electrodes were able to deliver the charge and remain functional as electrodes throughout the full 24 h of stimulation. Some changes in the electrodes were however measurable: the working electrode (*i.e.,* oxidizing anode) has a decreased CSC for all electrodes after long-term DC stimulation, yet remains much higher for the LIG/PP$_h$ electrodes in comparison to all the other electrodes. However, this change is not indicating failure of the electrode material, but rather is a consequence of ions being expelled from the anode and absorbed into the cathode. A polarity switch of electrodes was also performed in situ with the same PBS solution by simply exchanging the potentiostat's leads (Fig. 5c). The purpose was to show that the hydrogel can reversibly swell and shrink with similar potential profiles for the same given current density (25 μA/cm^2). Results proved that even after long-term DC stimulation, the ion-swelled PPh electrodes can effectively deliver charge to the ion-depleted electrodes even for 16 h (8 h in one direction then followed by another 8 h in the reverse direction), suggesting that direct current is injected via a reversible mechanism. The much thinner LIG/PP$_h$ electrode had a comparably similar electrical potential despite its pronounceably lower bulk volume compared to Ag/AgCl. This thinner nature allows for more flexibility and conformability such that it can provide a more encompassing contact to skin.

3.6. Myoelectric pattern recognition and stimulation threshold on human participants

A real-time myoelectric pattern recognition test and an electrical stimulation test for sensory perception were performed to evaluate the performance of the LIG/PP$_h$ electrodes in comparison to commercial Ag/AgCl electrodes, both for the recording and stimulation purposes. Six able-bodied participants had both LIG/PP$_h$ and Ag/AgCl electrodes positioned on the forearm (3 pairs of 2 electrodes of each type) and arranged in a crossed fashion, such that each electrode type had comparable positioning, as well as a common Ag/AgCl reference electrode (Fig. 6a).

The myoelectric pattern recognition classifier was trained to decode six different movements (open hand, close hand, flex hand, extend hand, pronation, and supination). After classifier training, the "Motion Test" was conducted (Ortiz-Catalan et al., 2013; Kuiken et al., 2009). The Motion Test is a match-prompt test, where the participant was prompted to match movements shown on a screen. The participants performed 30 trials per Motion Test, with each movement being randomized five times. This was performed for each electrode type and participants were blinded to which electrode type was being tested. The six participants completion rate (percentage of successful trials) and accuracy (percentage of correct movements predictions within a trial) were comparably successful for the LIG/PP$_h$ electrodes and the Ag/AgCl electrodes: 97.2 vs. 100.0% and 61.8 vs. 66.3%, respectively (Fig. 6d). The time needed for the classifier to select or call the movement was also comparable between LIG/PP$_h$ and Ag/AgCl electrodes: 0.74 vs. 0.64 s.

The perception threshold test was conducted in order to measure the lowest current that elicited perception. In this test, a participant would see two prompts (two-interval forced-choice). In one of the prompts, the participant received stimulation, and no stimulation in the other. After both prompts, the participant was asked which prompt contained the stimulation. Upon a correct answer, the amplitude of the stimulation was lowered (and vice versa upon an incorrect answer) according to a stochastic approximation staircase, and the test was repeated a total of 20 times (Fig. 6c). (Faes et al., 2007) The LIG/PP$_h$ electrodes had a lower threshold compared to Ag/AgCl: 370 vs. 546 μA, respectively. Thus, showing the former elicited sensations with less current (Fig. 6e). This feature is desirable since it would require less power in applications driven by batteries (*e.g.,* closed-loop prosthetic control systems with soft versus strong touch), while also providing a larger range for electrotactile stimulation which translates to higher resolution sensory feedback (*i.e.,* more levels of perception).

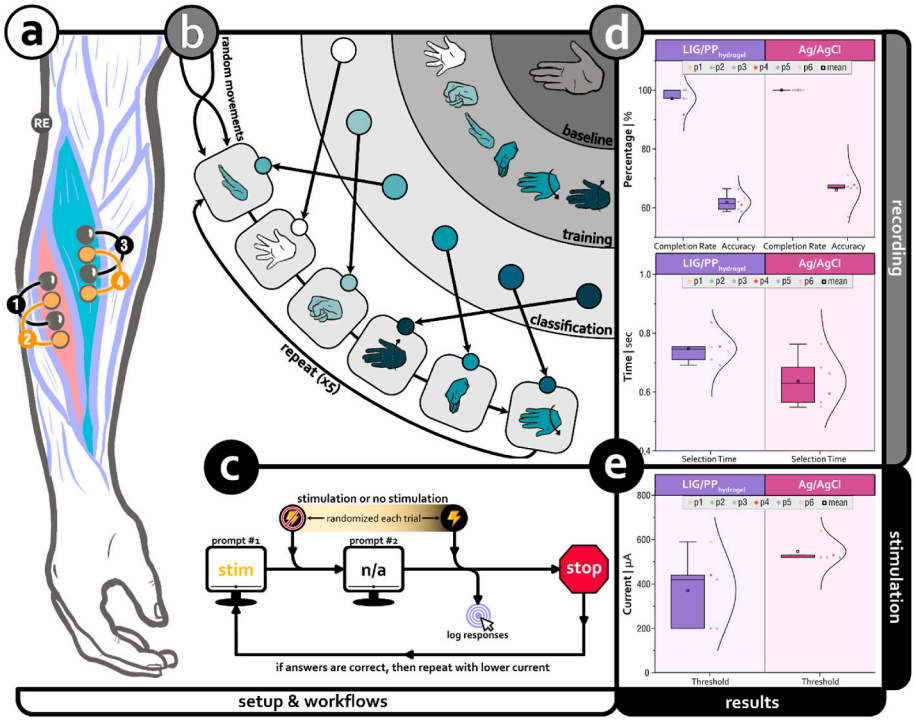

Fig. 6. Myoelectric pattern recognition and stimulation threshold comparison between LIG/PP$_h$ and Ag/AgCl electrodes. (a) Illustration of electrode pair placement on the participant's arm, where black electrodes are Ag/AgCl and orange are LIG/PP$_h$. **(b)** Workflow for the myoelectric pattern recognition test from training six hand movements to prompting participants to generate a series of random movements such that each hand movement is repeated six times and let the classifier to predict each movement based off the trained data. **(c)** Workflow for the perceivable stimulation threshold test where the participant is randomly either given a stimulation at a given current or not given any stimulation and if the participant answers correctly then the test is repeated at a lower current until failure. **(d)** Completion rate, accuracy, and selection time of myoelectric pattern recognition classifier for each electrode type. **(e)** lowest perceivable current threshold for each participant and each electrode type. (For interpretation of the references to colour in this figure legend, the reader is referred to the Web version of this article.)

4. Discussion

In this paper, three technological achievements were merged. Namely, the manufacturing of LIG electrodes, the addition of pure PEDOT:PSS hydrogels to buffer the interface between electrode and skin, and the surface functionalization allowing the two materials to be linked into an extremely reliable electrode complex. The linking between LIG and PEDOT:PSS hydrogels provided a way to mesh the field of inexpensive electrode patterning with economical biocompatible supercapacitors that enables stimulation and recording applications beyond EMG electrodes. In several aspects, such as process development, surface characterization, electrochemical performance, and recording and stimulating on human patients, the LIG/PP_h electrodes demonstrated to be a low-cost, patternable, process-scalable, and metal-free replacement to common Ag/AgCl electrodes.

Ag/AgCl electrodes with gel-based electrolytes continue to be the gold-standard in clinical settings due to their stable recordings that such non-polarizable electrode materials are known to provide. For applications beyond diagnostics, it is nevertheless common to use other electrode materials, even when these provide inferior signal quality in comparison to Ag/AgCl. For instance, when non-invasive biopotential recordings are used for control of external prosthetic systems, the application of electrodes to the skin needs to be simple, cheap to replace, and able to support stable recording conditions during everyday activities. If reasonable signal quality can be accomplished with a semi-dry skin-electrode contact, then it is more attractive than an electrode that may perform better in the short-term, but whose performance varies with hydration state of the gel or degrades due to the slow dissolution of the active layer of AgCl. In this light, these results demonstrate that LIG/PEDOT:PSS electrodes can perform at comparable levels to Ag/AgCl. This is already particularly promising and strongly supports the use of more modern materials for the growing application field of non-invasive bioelectronic applications.

Importantly, the LIG/PEDOT:PSS electrodes are not only able to compete with Ag/AgCl electrodes in recording performance, but furthermore are able to address a weakness of most metal electrodes. Specifically, they can be used for corrosion-free DC stimulation. Unbuffered or inadequately buffered Ag/AgCl electrodes can leech silver ions into tissue, which are known to be toxic *in vitro* and *in vivo* (Schopf et al., 2016; Zhao et al., 2021; Greulich et al., 2012). Whereas for PEDOT:PSS electrodes, they have proven to be superior in this regard, also both *in vitro* and *in vivo* (Leal et al., 2021; Boehler et al., 2017, 2019). Also, for traditional applications (*e.g.,* transcranial direct current stimulation – tDCS), the low input current of LIG/PP_h allows for less energy consumption during stimulation (Aplin and Fridman, 2019). The charge density demonstrated by the LIG/PP_h electrodes during long-term DC stimulation (8640 and 18,000 C/m^2 for 24 h at 10 μA/cm^2 and 20 h at 25 μA/cm^2, respectively) were well within the therapeutic window for tDCS for rats and humans (Liebetanz et al., 2009; Chhatbar et al., 2017). Also, the LIG/PPh electrodes showed a resilient shelf-life (*e.g.,* 18 months), even when pre-stressed and stored dry (Fig. S6). LIG-based electrodes have overwhelmingly been used for sensing, not stimulation (Kurra et al., 2019). However, it has been shown that LIG can be used for alternating current (AC) - based stimulation and even coupled with PEDOT:PSS thin films (Xu et al., 2018; Nair et al., 2020). As an extension to this AC stimulation, this work provides the first validation of using the combination of LIG and PEDOT:PSS hydrogel for long-term DC stimulation.

5. Conclusion

The transition from metals to carbon-based conducting materials is a crucial part in making biopotential electrodes a more generally accessible and affordable part of bioelectronic systems. In contrast to electrodes based on noble metal coatings, our solution mainly requires elements available in abundance in nature (hydrogen, carbon, oxygen), and the electrodes can be treated as disposable. Furthermore, it is not only a step towards making technology more affordable, but it notably offers improved perspectives for combining non-invasive biopotential recordings with other modalities (*e.g.,* magnetic resonance imaging – MRI) where current induction in metals is a substantial problem. With future work, extending the metal-free strategy also to the interconnection technology could fully enable LIG/PP_h as a conceivable application material for combined EEG, transcranial stimulation and MRI. Beyond the scope of stimulation electrodes, the functionalization of oxide groups on the LIG via O_2 plasma allows for further customization of the LIG itself (*e.g.,* other biochemical moieties), such as an electrochemical sensor layer.

The processes developed here provide a scalable and tailorable way to fabricate electrodes in the 0.1–100 mm feature size range with resolution mainly being limited by the precision of the laser carbonization process. This practical limitation could be overcome by using an alternative route for pyrolysis, as has been shown by Vomero et al. (2016), where the structures are patterned before the pyrolysis and then are embedded in the insulating polyimide. Future improvements of a more stretchable substrate would be desirable. For instance, the post-patterned LIG could be heat-transferred from polyimide into an elastomer thus more akin to other non-metal electrodes (Dallinger et al., 2020; Nilchian and Li, 2016). With these future potential adaptations, the concepts for adhesion promotion demonstrated here, stably linking LIG and PEDOT:PSS hydrogels, could be applied on electrodes with micrometer precision. This is worth noting as this efficiently addresses one of the known limitations with PEDOT:PSS based electrodes and could be of great use beyond the scope of non-invasive biopotential recordings.

Supporting Information

Supporting information is provided at the end of this document. This includes five figures and their descriptive text. Two movies are submitted via the submission portal, but the descriptive text is listed in the "Supporting Information" section at the bottom of this document.

CRediT authorship contribution statement

Sebastian W. Shaner: Conceptualization, Methodology, Investigation, Visualization, Writing – original draft, Writing – review & editing. **Monsur Islam:** Conceptualization, Methodology, Investigation, Visualization, Writing – original draft, Writing – review & editing. **Morten B. Kristoffersen:** Conceptualization, Methodology, Investigation, Writing – original draft, Writing – review & editing. **Raheleh Azmi:** Methodology, Investigation, Visualization, Writing – original draft, Writing – review & editing. **Stefan Heissler:** Investigation. **Max Ortiz-Catalan:** Conceptualization, Supervision, Funding acquisition, Writing – original draft, Writing – review & editing. **Jan G. Korvink:** Conceptualization, Supervision, Funding acquisition. **Maria Asplund:** Conceptualization, Supervision, Funding acquisition, Writing – review & editing.

Declaration of competing interest

The authors declare the following financial interests/personal relationships which may be considered as potential competing interests:

Sebastian Shaner, Maria Asplund reports financial support was provided by European Research Council. Jan Korvink, Monsur Islam reports financial support was provided by German Research Foundation. Max Ortiz-Catalan reports financial support was provided by Promobilia foundation. Max Ortiz-Catalan reports financial support was provided by IngaBritt and Arne Lundberg Foundation. Max Ortiz-Catalan reports financial support was provided by Swedish Research Council. Sebastian Shaner, Monsur Islam reports financial support was provided by Karlsruhe Institute of Technology Institute for Applied Materials.

Acknowledgements

This project was funded by the European Research Council (ERC) under the European Union's Horizon 2020 Research and Innovation program under grant agreement (No. 759655, SPEEDER). Funding from Deutsche Forschungsgemeinschaft (DFG, German Research Foundation) under Germany's Excellence Strategy via the Excellence Cluster 3D Matter Made to Order (EXC-2082/1–390761711) was used for work done by collaborators at the Karlsruhe Institute of Technology (KIT) in Eggenstein-Leopoldshafen, Germany. The Promobilila Foundation, the IngaBritt and Arne Lundbergs Foundation, and the Swedish Research Council (Vetenskapsrådet) provided funding for work done by collaborators at Chalmers University of Technology. We appreciatively acknowledge Albina Nirupa Julius from KIT (at the Institute of Microsystems Technology - IMT) for helping with contact angle measurements as well as Dr. Julia Maibach and Dr. Raheleh Azmi from KIT (at the Institute of Applied Materials – IAM and Karlsruhe Nano Micro Facility - KNMF) for performing the XPS of all the samples (No. 2019-023-027250 and 2020-024-029410).

Appendix A. Supplementary data

Supplementary data to this article can be found online at https://doi.org/10.1016/j.biosx.2022.100143.

References

Aplin, F.P., Fridman, G.Y., 2019. Front. Neurosci. 13, 379.
Asplund, M., Nyberg, T., Inganäs, O., 2010. Polym. Chem. 1 (9), 1374–1391.
Bae, E.J., Kang, Y.H., Jang, K.S., Cho, S.Y., 2016. Sci. Rep. 6, 18805.
Balint, R., Cassidy, N.J., Cartmell, S.H., 2014. Acta Biomater. 10 (6), 2341–2352.
Bareket, L., Inzelberg, L., Rand, D., David-Pur, M., Rabinovich, D., Brandes, D., Hanein, Y., 2016. Sci. Rep. 6 (1), 1–8.
Boehler, C., Kleber, C., Martini, N., Xie, Y., Dryg, I., Stieglitz, T., Hofmann, U.G., 2017. M.Asplund. *Biomater.* 129, 176–187.
Boehler, C., Oberrueber, F., Asplund, M., 2019. J. Contr. Release 304, 173–180.
Boehler, C., Carli, S., Fadiga, L., Stieglitz, T., Asplund, M., 2020. Nat. Protoc. 15 (11), 3557–3578.
Bredas, J.L., Street, G.B., 1985. Acc. Chem. Res. 18 (10), 309–315.
Chhatbar, P.Y., George, M.S., Kautz, S.A., Feng, W., 2017. Brain Behav. Immun. 66, 414.
Dallinger, A., Keller, K., Fitzek, H., Greco, F., 2020. ACS Appl. Mater. Interfaces 12 (17), 19855–19865.
Das, P.S., Hossain, M.F., Park, J.Y., 2017. Microelectron. Eng. 180, 45–51.
Faes, L., Nollo, G., Ravelli, F., Ricci, L., Vescovi, M., Turatto, M., Antolini, R., 2007. Percept. Psychophys. 69 (2), 254–262.
Ghosh, S., Rasmusson, J., Inganäs, O., 1998. Adv. Mater. 10 (14), 1097–1099.
Greczynski, G., Kugler, T., Salaneck, W.R., 1999. Thin Solid Films 354 (1–2), 129–135.
Greulich, C., Braun, D., Peetsch, A., Diendorf, J., Siebers, B., Epple, M., Köller, M., 2012. RSC Adv. 2 (17), 6981–6987.
Gueye, M.N., Carella, A., Faure-Vincent, J., Demadrille, R., Simonato, J.P., 2020. Prog. Mater. Sci. 108, 100616.
Han, D., Yang, G., Song, J., Niu, L., Ivaska, A., 2007. J. Electroanal. Chem. 602 (1), 24–28.
Hong, G., Lieber, C., 2019. Nat. Rev. Neurosci. 20.
Inoue, A., Yuk, H., Lu, B., Zhao, X., 2020. Sci. Adv. 6 (12), eaay5394.
Kim, J.H., Hwang, J.Y., Hwang, H.R., Kim, H.S., Lee, J.H., Seo, J.W., Shin, U.S., Lee, S.H., 2018. Sci. Rep. 8 (1), 1–11.
Kleber, C., Bruns, M., Lienkamp, K., Rühe, J., Asplund, M., 2017. Acta Biomater. 58, 365–375.
Kuiken, T.A., Li, G., Lock, B.A., Lipschutz, R.D., Miller, L.A., Stubblefield, K.A., Englehart, K.B., 2009. JAMA 301 (6), 619–628.
Kurra, N., Jiang, Q., Nayak, P., Alshareef, H.N., 2019. Nano Today 24, 81–102.
Leal, J., Jedrusik, N., Shaner, S., Boehler, C., Asplund, M., 2021. Biomater, 120949.
Lee, S., Kruse, J., 2009. Analog Devices 200, 1–2.
Lee, L., Kim, G.W., Yang, M., Kim, T.S., 2016. ACS Appl. Mater. Interfaces 8 (1), 302–310.
Liebetanz, D., Koch, R., Mayenfels, S., König, F., Paulus, W., Nitsche, M.A., 2009. Clin. Neurophysiol. 120 (6), 1161–1167.
Lu, B., Yuk, H., Lin, S., Jian, N., Qu, K., Xu, J., Zhao, X., 2019. Nat. Commun. 10 (1), 1–10.
Mamleyev, E.R., Heissler, S., Nefedov, A., Weidler, P.G., Nordin, N., Kudryashov, V.V., Länge, K., MacKinnon, N., Sharma, S., 2019. npj Flexible Electron 3 (1), 1–11.
Mamleyev, E.R., Falk, F., Weidler, P.G., Heissler, S., Wadhwa, S., Nassar, O., Shyam Kumar, C.N., Kübel, C., Wöll, C., Islam, M., Mager, D., Korvink, J.G., 2020. ACS Appl. Mater. Interfaces 12 (47), 53193–53205.
Mastinu, E., Håkansson, B., Ortiz-Catalan, M., 2017. IEEE BSN Conf 19–22.
Nair, V., Yi, J., Isheim, D., Rotenberg, M., Meng, L., Shi, F., Tian, B., 2020. Sci. Adv. 6 (34), eaaz2743.
Nasybulin, E., Wei, S., Kymissis, I., Levon, K., 2012. Electrochim. Acta 78, 638–643.
Naveen, M.H., Gurudatt, N.G., Shim, Y.B., 2017. Appl. Mater. Today 9, 419–433.
Nilchian, A., Li, C.Z., 2016. J. Anal. Chem. 781, 166–173.
Noh, Y., Bales, J.R., Reyes, B.A., Molignano, J., Clement, A.L., Pins, G.D., Florian, J.P., Chon, K.H., 2016. Ann. Biomed. Eng. 44 (8), 2464–2479.
Ortiz-Catalan, M., Brånemark, R., Håkansson, B., 2013. Source Code Biol. Med. 8 (1), 1–18.
Ouyang, L., Wei, B., Kuo, C.C., Pathak, S., Farrell, B., Martin, D.C., 2017. Sci. Adv. 3 (3), e1600448.
Parry, K.L., Shard, A.G., Short, R.D., White, R.G., Whittle, J.D., Wright, A., 2006. Surf. Interface Anal. 38 (11), 1497–1504.
Persson, K.M., Gabrielsson, R., Sawatdee, A., Nilsson, D., Konradsson, P., Berggren, M., 2014. Langmuir 30 (21), 6257–6266.
Schopf, A., Boehler, C., Asplund, M., 2016. Bioelectrochemistry 109, 41–48.
Scofield, J.H., 1976. J. Electron. Spectrosc. Relat. Phenom. 8 (2), 129–137.
Takeda, K., Tanino, G., Miyasaka, H., 2017. Med. Dev. Evid. Res. 10.
Tanuma, S.P., 1994. Surf. Interface Anal. 21, 165.
Thakor, N.V., 2015. Telehealth and Mobile Health, pp. 595–614.
Thakral, G., LaFontaine, J., Najafi, B., Talal, T.K., Kim, P., Lavery, L.A., 2013. Diabet. Foot Ankle 4, 22081.
Tomczykowa, M., Plonska-Brzezinska, M.E., 2019. Polymers 11 (2), 350.
Vomero, M., Van Niekerk, P., Nguyen, V., Gong, N., Hirabayashi, M., Cinopri, A., Logan, K., Moghadasi, A., Varma, P., Kassegne, S., 2016. J. Micromech. Microeng. 26 (2), 025018.
Vomero, M., Castagnola, E., Ciarpella, F., Maggiolini, E., Goshi, N., Zucchini, E., Carli, S., Fadiga, L., Kassegne, S., Ricci, D., 2017. Sci. Rep. 7 (1), 1–14.
Wang, Y., Alsmeyer, D.C., McCreery, R.L., 1990. Chem. Mater. 2 (5), 557–563.
Wirthl, D., Pichler, R., Drack, M., Kettlguber, G., Moser, R., Gerstmayr, R., Hartmann, F., Bradt, E., Kaltseis, R., Siket, C.M., Schausberger, S., Hild, S., Bauer, S., Kaltenbrunner, M., 2017. Sci. Adv. 3 (6), e1700053.
Xu, G., Jarjes, Z.A., Desprez, V., Kilmartin, P.A., Travas-Sejdic, J., 2018. Biosens. Bioelectron. 107, 184–191.
Ye, R., James, D.K., Tour, J.M., 2019. Adv. Mat. 31 (1), 1803621.
Yuk, H., Lu, B., Zhao, X., 2019. Chem. Soc. Rev. 48 (6), 1642–1667.
Zhang, W., Zhao, B., He, Z., Zhao, X., Wang, H., Yang, S., Wu, H., Cao, Y., 2013. Energy Environ. Sci. 6 (6), 1956–1964.
Zhao, Y., Bunch, T.D., Isom, S.C., 2021. PLoS One 16 (2), e0246847.
Zielke, U., Hüttinger, K.J., Hoffman, W.P., 1996. Carbon 34 (8), 983–998.

Further reading

Benoudjit, A., Bader, M., Salim, W.W.A.W., 2018. Sens. Bio-Sens. Res. 17, 18–24.